AGU PUBLICATIONS

JGR

Journal of Geophysical Research: Space Physics

RESEARCH ARTICLE

10.1002/2016JA022882

Special Section:
Geospace system responses to the St. Patrick's Day storms in 2013 and 2015

Key Points:
- Upward ion drifts are responsible for the throat region SED formation
- Horizontal ion drifts play an essential role in forming TOIs
- SED/TOI for these two March storms have quite close UT occurrences

Correspondence to:
J. Liu,
jingliu@ucar.edu

Citation:
Liu, J., W. Wang, A. Burns, S. C. Solomon, S. Zhang, Y. Zhang, and C. Huang (2016), Relative importance of horizontal and vertical transports to the formation of ionospheric storm-enhanced density and polar tongue of ionization, *J. Geophys. Res. Space Physics*, *121*, 8121–8133, doi:10.1002/2016JA022882.

Received 28 APR 2016
Accepted 10 AUG 2016
Accepted article online 11 AUG 2016
Published online 30 AUG 2016

Relative importance of horizontal and vertical transports to the formation of ionospheric storm-enhanced density and polar tongue of ionization

Jing Liu[1], Wenbin Wang[1], Alan Burns[1], Stanley C. Solomon[1], Shunrong Zhang[2], Yongliang Zhang[3], and Chaosong Huang[4]

[1]High Altitude Observatory, National Center for Atmospheric Research, Boulder, Colorado, USA, [2]Haystack Observatory, Massachusetts Institute of Technology, Westford, Massachusetts, USA, [3]Space Department, Applied Physics Laboratory, Johns Hopkins University, Baltimore, Maryland, USA, [4]Air Force Research Laboratory, Kirtland AFB, Albuquerque, New Mexico, USA

Abstract There are still uncertainties regarding the formation mechanisms for storm-enhanced density (SED) in the high and subauroral latitude ionosphere. In this work, we deploy the Thermosphere Ionosphere Electrodynamic General Circulation Model (TIEGCM) and GPS total electron content (TEC) observations to identify the principle mechanisms for SED and the tongue of ionization (TOI) through term-by-term analysis of the ion continuity equation and also identify the advantages and deficiencies of the TIEGCM in capturing high-latitude and subauroral latitude ionospheric fine structures for the two geomagnetic storm events occurring on 17 March 2013 and 2015. Our results show that in the topside ionosphere, upward $\mathbf{E}\times\mathbf{B}$ ion drifts are most important in SED formation and are offset by antisunward neutral winds and downward ambipolar diffusion effects. In the bottomside *F* region ionosphere, neutral winds play a major role in generating SEDs. SED signature in TEC is mainly caused by upward $\mathbf{E}\times\mathbf{B}$ ion drifts that lift the ionosphere to higher altitudes where chemical recombination is slower. Horizontal $\mathbf{E}\times\mathbf{B}$ ion drifts play an essential role in transporting plasma from the dayside convection throat region to the polar cap to form TOIs. Inconsistencies between model results and GPS TEC data were found: (1) GPS relative TEC difference between storm time and quiet time has "holes" in the dayside ion convection entrance region, which do not appear in the model results. (2) The model tends to overestimate electron density enhancements in the polar region. Possible causes for these inconsistencies are discussed in this article.

1. Introduction

Several prominent ionosphere structures occur at high latitudes and in subauroral regions during geomagnetic storms. These include subauroral polarization streams (SAPS), storm time-enhanced density (SED), tongue of ionization (TOI), and boundary blobs (see Figure 1). These structures are very dynamic because electric fields and particle precipitation of magnetospheric origin and their associated energy and momentum deposition into the upper atmosphere are highly variable during the storms.

Storm time, single-site observations from the Millstone Hill Incoherent Radar (ISR) frequently show dramatic *F* region electron density enhancements around the duskside, which is termed the "dusk effect" [e.g., *Papagiannis et al*., 1971; *Mendillo et al*., 1972; *Evans*, 1973; *Anderson*, 1976; *Buonsanto*, 1995a, 1995b, 1999]. Based on Millstone Hill ISR 2-D electron density measurements, *Foster* [1993] renamed this phenomenon SED, which is typically characterized by a latitudinally distinct region of sunward convection *F* region plasma, high electron densities, an elevated *F* region peak, a significantly enhanced topside ionosphere, and low electron temperatures near sunset at middle latitudes [*Foster*, 1993; *Liu et al*., 2015, 2016]. *Cherniak and Zakharenkova* [2015] reported that high-latitude ionospheric irregularities tend to occur in the edge of SED/TOI having steep ionospheric density gradients during the St. Patrick's Day event in 2015.

There are several different mechanisms proposed for the formation of the SED, including local upward $\mathbf{E}\times\mathbf{B}$ drifts [e.g., *Huang et al*., 2005; *Deng and Ridley*, 2006; *Heelis et al*., 2009; *David et al*., 2011; *Zou et al*., 2014], westward ion transport from the nightside to the dayside by SAPS [*Foster et al*., 2007], equatorward blowing neutral winds [*Anderson*, 1976], and latitudinal expansion of the equatorial ionization anomaly [e.g., *Kelley et al*., 2004; *Tsurutani et al*., 2004]. *Kelley et al*. [2004] and *Tsurutani et al*. [2004] thought that upward and meridional transport of equatorial *F* region plasma by a large storm time $\mathbf{E}\times\mathbf{B}$ drift and ambipolar diffusion

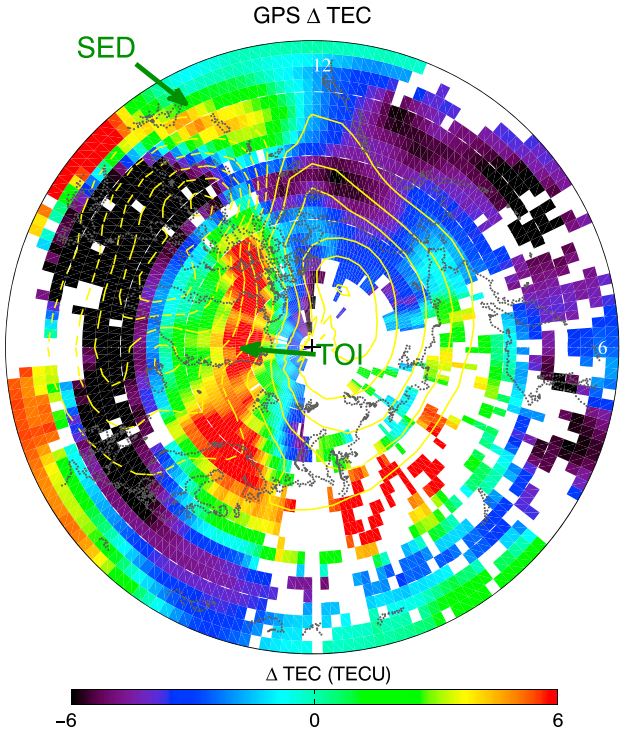

Figure 1. Polar view of absolute GPS TEC difference between storm time (2000 UT 17 March 2013) and quiet time (2000 UT 16 March 2013).

along the magnetic field lines were responsible for the SED generation. This mechanism was rejected by *Rishbeth et al.* [2010] because of the huge discrepancy that exists between the plasma lifetime and meridional transport time. *Rishbeth et al.* [2010] pointed out that local production, rather than remote latitudinal transport, should be the dominant cause. *Foster* [1993] showed that the expanded high-latitude convection electric fields in the postnoon sector continuously encounter fresh solar-produced plasma on the equatorward edge of the convection pattern and generate a latitudinally narrow region of SED in front of the expanded convection pattern. Based on the time-dependent ionosphere model simulation, *Heelis et al.* [2009] suggested that the expanded two-cell convection pattern gives rise to poleward and upward flow that raises the ionosphere to higher altitudes, where chemical recombination is slower. This is augmented by the fact that the westward flows are in the opposite direction with respect to Earth corotation. This produces zonal flow stagnation at a specific local time in the afternoon sector. TEC will be greatly increased under the conditions of plasma zonal motion stagnation and upward drifts in the sunlit. The large sunward flux carried by SAPS was also thought to be very important for SED [*Foster et al.*, 2007]. However, this was questioned by *Fuller-Rowell* [2011] based on the fact that fast ion flow carried by SAPS, in which electron density is already low, tends to further decrease the electron density as a result of increased frictional heating and so cannot provide a source for SED. Another explanation for the SED was a combined effect of westward ion drifts and equatorward neutral winds that forces plasma up along magnetic field lines reducing chemical recombination [*Anderson*, 1976].

SED provides a source for the polar cap TOI that is a large-scale (~1000 km) "tongue"-like enhanced plasma density structure carried by antisunward plasma flow and elongated in the noon-midnight direction [*Sato*, 1959]. In some literatures, people do not distinguish between SED and TOI since these two are quite similar but occur at different latitudes. However, *Liu et al.* [2015] reported that TOI can also occur during geomagnetic quiet or weakly disturbed conditions at favorable universal local times independent of SED occurrence. TOI tends to form during the universal times when high-latitude two-cell convection patterns are closer to solar-produced middle-latitude plasma source region, facilitating the poleward plasma transportations. The polar cap enhancement sometimes takes the form of a continuous TOI and sometimes as discrete patches. The SED/TOI has often been seen to segment into patches [e.g., *Lockwood and Carlson*, 1992; *Rodger et al.*, 1994; *Moen et al.*, 2008; *Zhang et al.*, 2011, 2013a, 2013b, 2015].

To sum up, the key issue regarding the SED formation mainly is which of the following proposed mechanisms is the dominant process: horizontal (westward) transport by SAPS and the auroral convection pattern, vertical upward $\mathbf{E}\times\mathbf{B}$ ion drifts, or equatorward blowing neutral winds. The objectives of this work are (1) to identify the main mechanism responsible for SED and TOIs and (2) to test the performance of the high-resolution TIEGCM in capturing the storm time polar ionospheric large-scale structures such as SED and TOI. Previous numerical modeling work related to SED or TOI has mostly used stand-alone ionosphere models, which lack of self-consistent thermosphere and ionosphere, and electrodynamics. This work will be the first attempt to utilize a 3-D, coupled ionosphere-thermosphere model to uncover the formation mechanism of SED and TOIs.

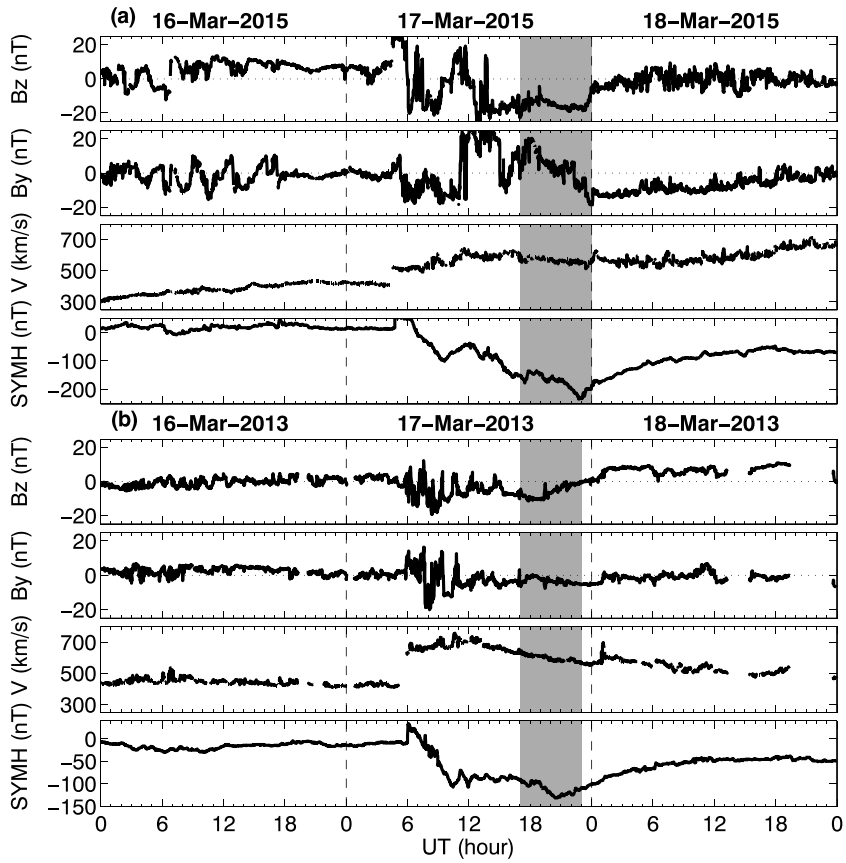

Figure 2. (a, b) IMF B_z (first row), B_y (second row), solar wind velocity (third row), and symmetric ring current index (*SYM-H*) (fourth row) for 16–18 March 2015 and 2013.

2. Model and Data

The NCAR-TIEGCM is a time-dependent, three-dimensional, thermosphere-ionosphere coupled model using the finite differencing technique to obtain a self-consistent solution for thermospheric and ionospheric dynamics, the associated dynamo electric field and currents [*Roble et al*., 1988; *Richmond et al*., 1992; *Qian et al*., 2014]. The high-resolution TIEGCM model used in the current work has 2.5° × 2.5° horizontal resolution and has 60 pressure surfaces in altitude ranging from 97 km to ~ 500 km, with a vertical resolution of one-fourth scale height. The input parameters for the TIEGCM are solar EUV and UV spectral fluxes, parameterized by the $F_{10.7}$ cm index, and high-latitude auroral particle precipitation [*Roble and Ridley*, 1987] and a convection electric field [*Weimer*, 2005]. The amplitudes and phases of tides from the lower atmosphere are specified by the global scale wave model at the model's lower boundary [*Hagan and Forbes*, 2002, 2003].

The 1 min resolution solar wind parameters are provided by the OMNI 2 database. The solar wind data have been shifted to the magnetopause [*King and Papitashvili*, 2005]. The ionospheric TEC data with a 5 min resolution were obtained from the Madrigal database. We refer to *Rideout and Coster* [2006] for a detailed description of this database.

3. Observations and Results

3.1. Interplanetary Solar Wind and Geomagnetic Activity Observations

Figure 2 shows the interplanetary solar wind parameters in the Geocentric Solar Magnetospheric coordinate system and geomagnetic activity index for the two storm cases during 16–18 March 2015 (Figure 2a) and 16–18 March 2013 (Figure 2b). In each case, panels from the top to bottom are interplanetary magnetic field (IMF) B_z and B_y components, solar wind velocity (*V*), and the symmetric ring current index (*SYM-H*). *SYM-H*

can be viewed as a high-resolution equivalence of the magnetic storm index *Dst*. The shaded areas denote the interval of SED or TOIs. *Liu et al*. [2016] gave a detailed description to the solar wind and geomagnetic disturbed conditions during the 17 March 2015 event. The interplanetary shock reached the magnetosphere at ~ 0430 UT on 17 March 2015, inducing a sudden storm commencement as indicated by the step-like increase in *SYM-H*. A strong southward turning of IMF B_z (~20 nT) occurred at around 0600 UT on 17 March 2015 resulting in the onset of the storm main phase. The *SYM-H* index reached a minimum value of −234 nT at ~ 2219 UT.

For the 17 March 2013 event, a shock impinged on the magnetosphere and triggered the sudden storm commencement at 0600 UT, after which IMF B_z was mostly southward with the solar wind velocity remaining at a relatively large value around 700 m/s. *SYM-H* attained a minimum value of −132 nT at ~ 2000 UT, after which IMF B_z began to turn northward.

These two storms share common features in storm onset and evolution but differ in storm intensity with the *SYM-H* index of −234 nT and −132 nT for the 2015 and 2013 storms, respectively. Both storms began at ~ 0600 UT on 17 March, then experienced a two-step decrease in the *SYM-H* index, and started to recover during 2200–2300 UT. Due to the great similarities between these two storms, they provide us a natural case to do comparative studies.

3.2. GPS TEC Observations and TIEGCM Simulations

Figure 3 illustrates the absolute difference between storm time (17 March) and quiet time (16 March) TEC during 1600–2200 UT, corresponding to the later main phase and early recovery phase of the two geomagnetic storm events. Figures 3 (left column) and 3 (right column) correspond to the 2015 and 2013 storm events, respectively. At 1600 UT for the 2015 storm event, a positive storm effect (TEC enhancement) appeared at middle and low latitudes in the American longitudes and the western side of Europe. For the 2013 storm case, a negative storm effect (TEC depletion) was obvious in the low-latitude and equatorial ionosphere. For both events, the negative ionospheric storm effects dominated the high-latitude ionosphere. These negative ionospheric effects were much stronger in the 2015 storm than they were in the 2013 storm.

Two hours later (1800 UT), as pointed by *Liu et al*. [2016], a SED feature could be identified as a tiny enhanced TEC structure within the 40–60° latitudinal ranges over the east coast of Canada on 17 March 2015. This feature occurred over the North Atlantic Ocean during the 2015 event but was not seen during the 2013 event. At 1800 UT during the 2015 event, negative storm effects were stronger than they were 2 h earlier. For the 2013 storm case, middle-latitude daytime positive storm effects were further enhanced in the NH. Both storms exhibited hemispheric asymmetry in response to the storm. For example, we can see that the high-latitude negative storm effect in the Northern Hemisphere (NH) was stronger and spread more equatorward than that in the Southern Hemisphere (SH) for the 2015 storm event. For the same event, the daytime TEC enhancement in the NH moved to higher latitudes. Similarly, the TEC enhancements in the SH also moved to higher latitudes over the ocean where no TEC data were available.

At 2000 UT during the 2015 event, the SED signature became more evident, progressing further toward the magnetic pole than it was 2 h earlier. At the same time, the negative ionospheric storm effect expanded further equatorward and became more intense compared with the effect at 1800 UT. For the 2013 storm event, a TOI feature, characterized by the increased TEC in the 50–80° latitude ranges, originated almost from the same location as the SED in the 2015 storm event and ended over Northern Russia at 2300 LT (not shown).

At 2200 UT, there were no obvious changes in the global pattern for the 2015 event, except for the weakened SED compared to 2000 UT. For the 2013 storm event, the TOI was cut off by a negative storm effect close to the NH magnetic pole.

To sum up these two storms, the daytime ionospheric response was characterized by high-latitude negative storm effects and low-latitude positive storm effects. The reduced electron content at high latitudes and increased TEC at middle latitudes exhibited hemispheric asymmetry even though they took place very close to the March equinox. Negative ionospheric storm effects occur frequently over the dip equator in the daytime, which may be related to the eastward penetration electric field together with a horizontal magnetic field producing upward vertical drifts that leads to decreases in electron density after these electrons diffuse down field lines. The postmidnight ionosphere was dominated by TEC depletion. TOIs originated from the

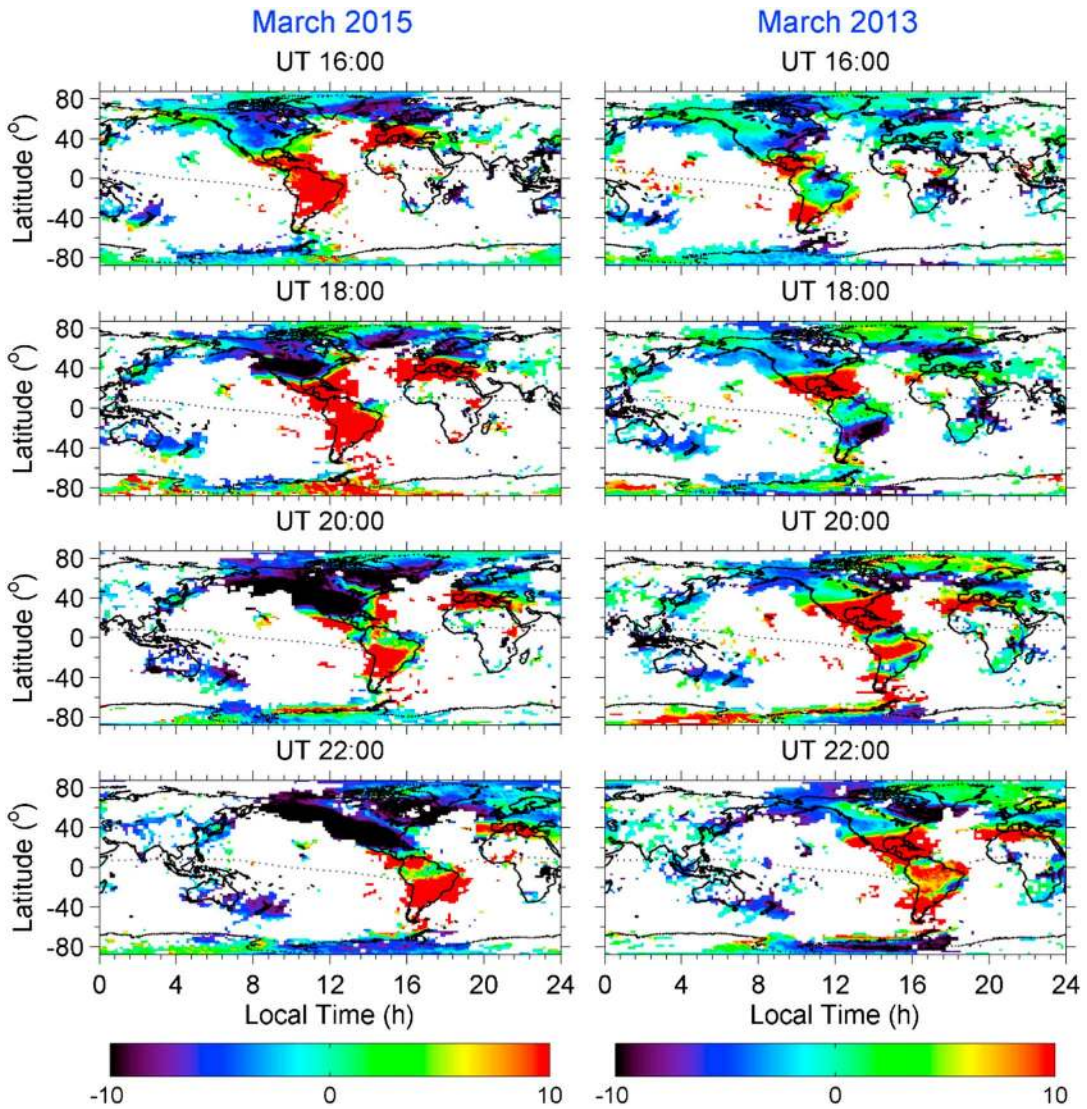

Figure 3. Absolute TEC difference between storm time (17 March) and quiet time (16 March) for 2015 (left column) and 2013 (right column).

middle-latitude TEC enhancements and were conjugate phenomena. It is interesting to note that TOIs were conjugate but the negative storm effect at high latitudes was hemispherically asymmetric. This is due to the fact that TOIs are mostly ordered in magnetic coordinates, while the negative storm effects are caused by O/N_2 changes that are strongly affected by neutral winds. Neutral winds are not necessarily configured in the magnetic coordinate system.

Figure 4 compares the absolute TEC differences between storm (17 March 2015) and quiet times (16 March 2015) from GPS observations (left column) and TIEGCM simulations (right column) in polar geographic coordinates. The outer circle corresponds to 40° geographic latitude. The model tends to overestimate positive ionospheric storm effects and underestimate negative ionospheric storm effects in the polar ionosphere, which could be related to the underestimation of Joule Heating and the resultant smaller decrease in O/N_2, or an excess of soft particle precipitation, or too many secondary electrons in the upper parts of the model. For example, a clear TOI signature extending from the daytime throat region to the postmidnight auroral oval region along the noon-midnight meridian section can be seen in the model results, but it is significantly weaker in the observations. In addition, at 1800 and 2000 UT, there is an electron density "hole" at geographic latitudes of 60–70° in the afternoon sector. We have found that the hole in the difference field between storm and quite TEC in the throat region of the convection pattern occurs as a result of the quiet

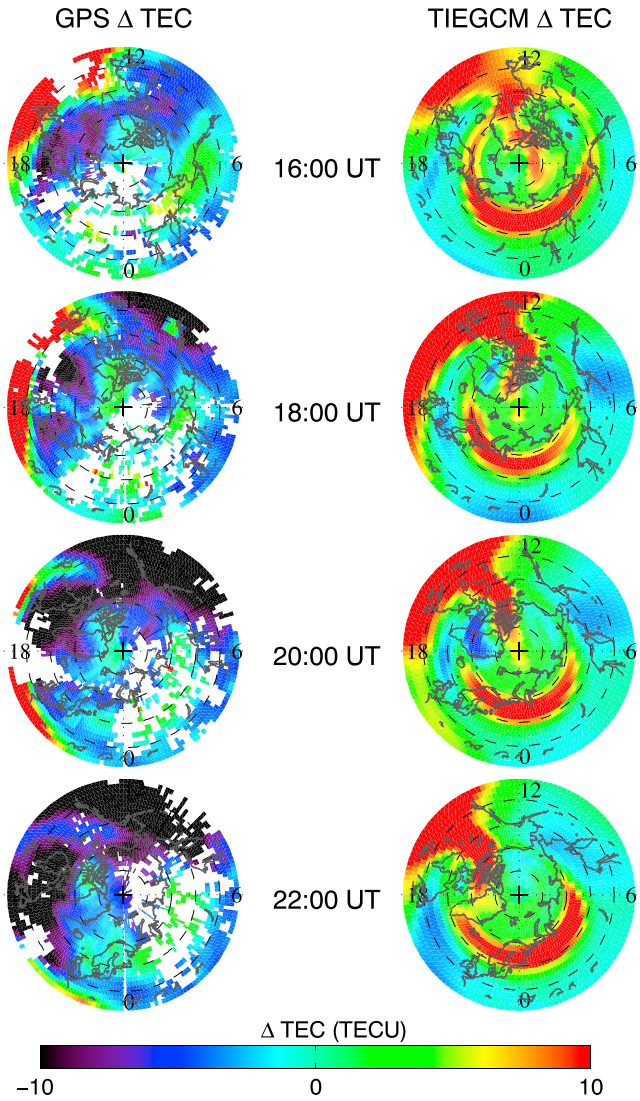

Figure 4. Polar view of absolute TEC difference between storm time (17 March 2015) and quiet time (16 March 2015).

day having enhanced TEC, not because there is a "hole" in the disturbed day TOI. There was also a weakly enhanced, TOI-like feature in GPS TEC in the polar cap.

Figure 5 is in the same format as Figure 4 but for the March 2013 storm event. The model captured the polar TOI signature in this event. As can be seen from the observations, a TOI signature appeared at around 1800 UT and a weak auroral boundary blob (enhanced TEC) occurred in the 60–70° geographic latitude range in the postmidnight sector. Again, it seems that the afternoon and morning sector negative ionospheric storm effects merged in the throat region in the GPS data, which separated the TOI from the middle-latitude source region. This feature is not as strong in model simulations as model underestimated the negative storm effect too in this event.

Overall, the model can roughly capture the TOI pattern and dynamics, but some discrepancies exist in the magnitude—the model tends to overestimate the strength of the TOI. We will use the model to diagnose the SED and TOI signatures.

Figure 6 shows absolute differences of the modeled F_2 layer peak density (N_mF_2), peak height (h_mF_2), neutral velocities, ion drifts, and O/N_2 at 2000 UT between storm time and quiet time for the March 2015 (left column) and 2013 (right column) events. A salient feature was the pronounced two-cell ion convection pattern, while neutral winds behaved in a similar way. A neutral O/N_2 "tongue" also was modeled in the 2015 event along the noon-midnight meridian; a similar phenomenon was reported by *Burns et al.* [2004]. The formation of a neutral "tongue" is mainly due to the poleward advection of middle-latitude air parcels that are rich in O/N_2. The frequent neutral-plasma collisions forced neutrals to move antisunward with the ions. As expected, the TOI signature also appeared in N_mF_2, similar to that in TEC. h_mF_2 increased by about 80–100 km in the noon throat region, which was accompanied by upward ion drifts.

3.3. Term Analysis of Formation Mechanisms for SED/TOI

Term analysis of the ion continuity equation was performed to identify the relative importance between the electric fields, neutral winds, chemical reactions, and ambipolar diffusion in generating SED/TOIs. The same method has also been used in other research [e.g., *Buonsanto*, 1995a; *Lei et al.*, 2008]. Because O^+ is the major ion species in the F_2 region, we carry out a term-by-term analysis of the O^+ continuity equation as follows.

$$\frac{\partial N_{O^+}}{\partial t} = q_{O^+} - \beta N_{O^+} - \nabla\cdot\left(N_{O^+}\vec{V}\right)$$

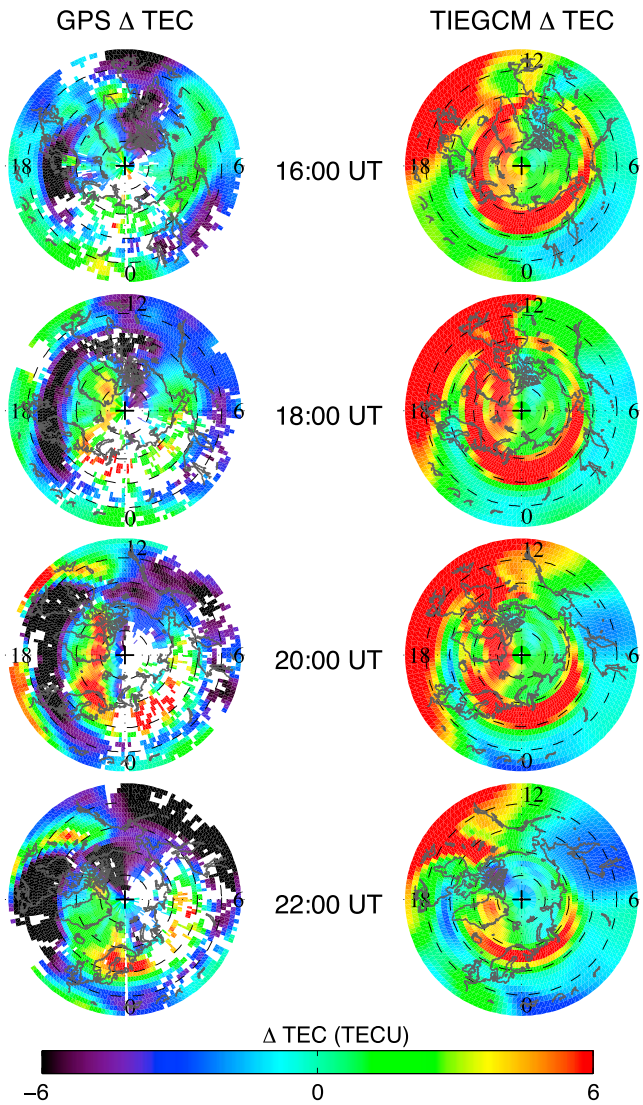

Figure 5. Polar view of absolute TEC difference between storm time (17 March 2013) and quiet time (16 March 2013).

In this equation, N_{O^+}, q_{o^+}, $\rightharpoonup V$, and β are the O^+ density, production rate, ion velocity, and loss coefficient, respectively. The left-hand side term represents the change rate of O^+ density with time, which is almost equal to the change rate in electron density in the *F* region. βN_{O^+} on the right-hand side is the loss rate. The last term $\nabla\cdot(N_{O^+}\rightharpoonup V)$ on the right-hand side includes the effects of neutral wind transport, $\mathbf{E}\times\mathbf{B}$ transport, and ambipolar diffusion. Furthermore, $\mathbf{E}\times\mathbf{B}$ transport can be decomposed into electric fields induced horizontal and vertical transports. In the term analysis, we bin the production and loss rates together as a chemical term. For convenience, the electron density change rate (δNE) induced by chemical production and loss rates, neutral wind transport, $\mathbf{E}\times\mathbf{B}$ transport, $\mathbf{E}\times\mathbf{B}$ induced horizontal transport, $\mathbf{E}\times\mathbf{B}$ induced vertical transport (δNE), and ambipolar diffusion were termed as δNE_{ch}, δNE_{w}, $\delta NE_{E\times B}$, $\delta NE_{E\times B\_hor}$, $\delta NE_{E\times B\_ver}$, and δNE_{Ambi_diff}, respectively. Thus, we have

$$\delta NE = \delta NE_{ch} + \delta NE_{w} + \delta NE_{E\times B} + \delta NE_{Ambi\_diff}$$

or

$$\delta NE = \delta NE_{ch} + \delta NE_{w} + \delta NE_{E\times B\_hor} + \delta NE_{E\times B\_ver} + \delta NE_{Ambi\_diff}$$

Figure 7 shows the absolute difference between storm time (17 March) and quiet time (16 March) electron density (ΔNE, first column, in units of 10^5 cm^{-3}), electron density change rate caused by production and loss ($\Delta\delta NE_{ch}$, second column, in units of cm^{-3} s^{-1}), neutral wind transport ($\Delta\delta NE_{w}$, third column, in units of cm^{-3} s^{-1}), electric field transport ($\Delta\delta NE_{E\times B}$, fourth column, in units of cm^{-3} s^{-1}), and ambipolar diffusion ($\Delta\delta NE_{Ambi_diff}$, fifth column, in units of cm^{-3} s^{-1}) at 2000 UT for both March 2015 (first and second rows) and March 2013 events (third and fourth rows). As shown in this figure, a TOI occurred both in the topside (pressure level 3.125; ~ 400 km) and bottomside (pressure level 1.125, ~ 280 km) ionosphere. The photochemical reaction process increases the bottomside ionosphere electron density in the nightside auroral oval but does not change the topside ionosphere very much. The altitudinal dependence of *F* region photochemical reaction is mainly due to the fact that the chemical production and loss of plasma is related to O and N_2, both of which decrease with altitude. This leads to a less impact of chemical reaction process at higher altitudes.

As shown in Figure 7 (third column), the neutral winds in the throat region decrease the electron density in the topside ionosphere and increase the electron density in the bottomside. The magnetospherically imposed electric fields cause antisunward plasma flow in the throat region, which, in turn, forces neutral winds to flow in the same direction due to frequent neutral-plasma collisions [e.g., *Deng and Ridley*, 2006]. These poleward neutral winds, in conjunction with inclined magnetic field lines, move the plasma downward

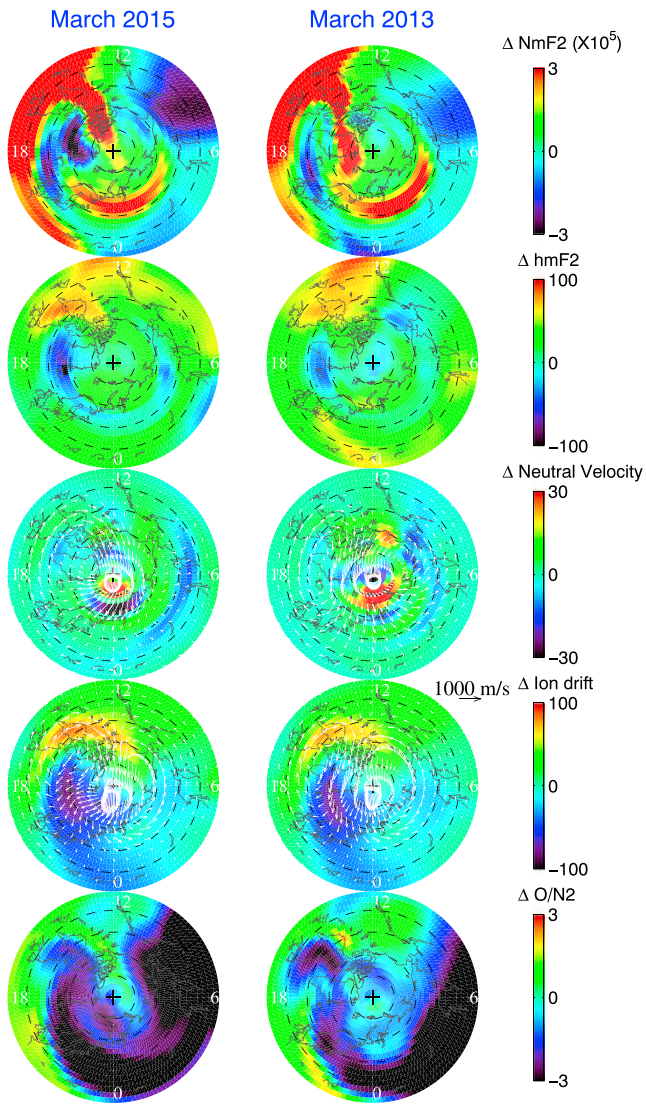

Figure 6. Polar view of modeled absolute difference between storm time (17 March) and quiet time (16 March) in N_mF_2, h_mF_2, neutral wind velocity, ion drifts and O/N_2 at 2000 UT for 2015 (left column) and 2013 (right column). The background in the third and fourth rows denotes the vertical wind and ion drifts, respectively.

and thus reduce the plasma content in the topside ionosphere. In addition, upwelling of air will lead to decreases in O/N_2 and resultant depletion in the topside ionosphere and cancel the driving force for the downward plasma motion.

In Figure 7 (fourth column), electric field transportation in the topside ionosphere increases ion density on the noonside and decreases it on the midnightside along the noon-midnight meridional direction. This can be interpreted from the fact that the expanded two-cell convection introduces eastward and westward electric fields at around the noon and midnight sectors, respectively. The $\mathbf{E}\times\mathbf{B}$ ion drifts are upward on the dayside and downward on the nightside [*Deng and Ridley*, 2006]. Therefore, these processes in the topside ionosphere lead to the dayside throat region electron density enhancement and midnight electron density depletion.

Ambipolar diffusion, which depends on gravity and the pressure gradient force, acts as a passive process mediating other physical processes. Generally, in Figure 7 (fifth column), the magnitudes of ambipolar diffusion-induced ion density changes are weaker than those due to neutral winds and electric fields. Ambipolar diffusion decreases the ion density in the topside ionosphere and increases it in the bottomside ionosphere. This could be related to the enhanced plasma density or temperature in the topside ionosphere as a result of external heating sources, which could quicken downward diffusion [*Lei et al.*, 2008; *Zou et al.*, 2014].

In general, in the topside ionosphere, the dominant mechanism leading to SED is electric field transport, which is offset by ambipolar diffusion and neutral wind transport. In the bottomside ionosphere, neutral winds play a major role in producing the SED structure, augmented by ambipolar diffusion and balanced by electric field transport. Integrated electron content mainly comes from the topside ionosphere [e.g., *Belehaki and Tsagouri*, 2002; *Liu et al.*, 2016]. So we further decompose the electric field effects on the topside ionosphere into horizontal and vertical directions.

Figure 8 illustrates the absolute differences in electron density rate of change between storm time and quiet time caused by electric fields transport ($\Delta\delta NE_{E\times B}$), electric fields induced horizontal transport ($\Delta\delta NE_{E\times B\_hor}$), and electric fields induced vertical transport ($\Delta\delta NE_{E\times B\_ver}$). Apparently, vertical transport is important for the SED in the throat region, whereas horizontal transport is more important in the polar cap region. This seems not to be consistent with traditional viewpoint that SED is generated near dusk and transported by horizontal

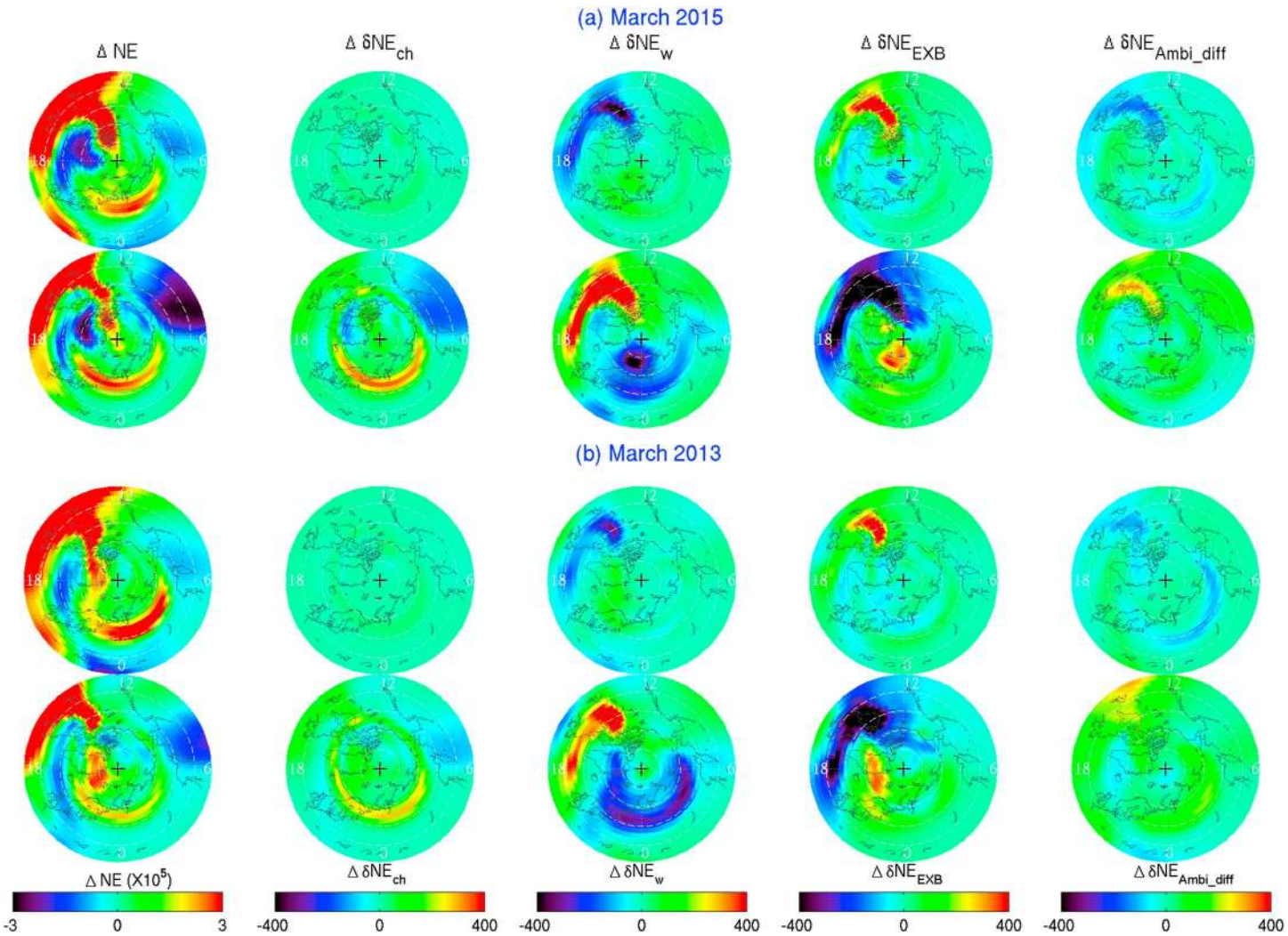

Figure 7. The modeled absolute difference between storm time (17 March) and quiet time (16 March) electron density (in units of 10^5 cm^{-3}) and electron density change rate caused by chemical processes ($\Delta\delta NE_{ch}$), neutral wind transport ($\Delta\delta NE_w$), electric field transport ($\Delta\delta NE_{E\times B}$), and ambipolar diffusion ($\Delta\delta NE_{Ambi\_diff}$) terms (in units of cm^{-3} s^{-1}) at 2000 UT for (a) March 2015 and (b) March 2013. The first and third rows denote the terms at pressure level 3.125 (~400 km), and the second and fourth rows are for the terms at pressure level 1.125 (~280 km).

plasma drifts to the dayside throat region. The model calculation of Figure 8 includes both local processes and global transport of ionospheric plasma. The source of the plasma density increase in the throat region is mostly due the upward motion of the local plasma. Why is vertical transport important in the dayside throat region? This is because that $\mathbf{E}\times\mathbf{B}$ ion drifts have a large upward vertical component on the dayside throat region given the large zonal electric fields in the presence of inclined magnetic field lines there [*Deng and Ridley*, 2006].

Figure 9 illustrates latitude slice of the absolute difference in electron density change (ΔNE, first row, in units of 10^5 cm^{-3}) between storm time and quiet time caused by these terms (in units of cm^{-3} s^{-1}): production and loss rates ($\Delta\delta NE_{ch}$, second row), neutral wind transport ($\Delta\delta NE_w$, third row), ambipolar diffusion ($\Delta\delta NE_{Ambi\_diff}$, forth row), electric fields transport ($\Delta\delta NE_{E\times B}$, fifth row), electric field horizontal transport ($\Delta\delta NE_{E\times B\_hor}$, sixth row), and electric field vertical transport ($\Delta\delta NE_{E\times B\_ver}$, seventh row) at 2000 UT. This figure gives the latitudinal slice at 1400 LT when the SED appeared at this UT. The left side panels are for the 2015 storm event, and the right side panels are for the 2013 storm event. According to Figure 5, the SED mainly occurs in the 50–60° geographic latitude range at 1400 LT. Figure 9 shows that electron density enhancements mainly occur at altitudes from 250 to 450 km. Weak enhancement can be observed at

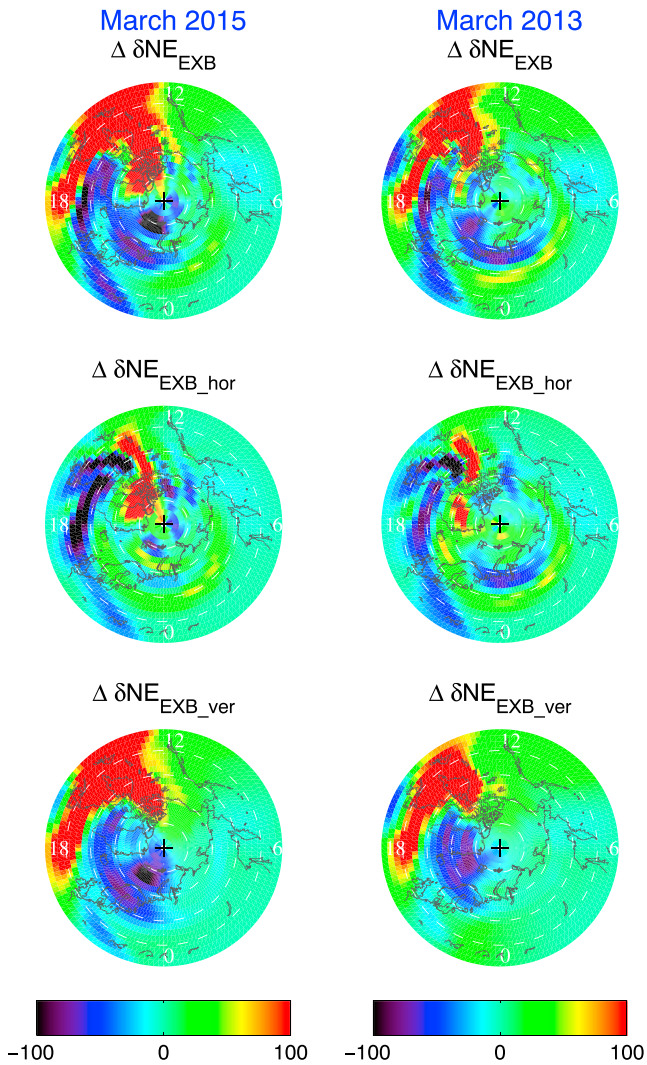

Figure 8. Modeled absolute difference in change rate of electron density between storm time (17 March) and quiet time (16 March) electron density change rate caused by electric fields transport ($\Delta\delta NE_{E\times B}$), electric fields induced horizontal transport ($\Delta\delta NE_{E\times B\_hor}$), and electric fields induced vertical transport ($\Delta\delta NE_{E\times B\_ver}$) terms (in units of $cm^{-3}\,s^{-1}$) at 2000 UT for (left column) 2015 and (right column) 2013.

240–320 km caused by the net effect of production and loss ($\Delta\delta NE_{ch}$). $\Delta\delta NE_{w}$ decreases ion densities at altitudes between 320 and 500 km and increases them between 200 and 300 km. TEC enhancements in the throat (50–60°) are mainly caused by the $\Delta\delta NE_{E\times B\_ver}$, whereas $\Delta\delta NE_{E\times B\_hor}$ plays a less important role in its formation in this region.

4. Discussion

As shown in Figures 7–9, SED/TOIs both occur in the bottomside and topside ionosphere. In the bottomside ionosphere, neutral winds play the decisive role in generating SED with contributions from ambipolar diffusion. This is because the antisunward neutral winds in the throat region have a downward component and increase the plasma in the bottomside ionosphere but decrease it in the topside. However, $\mathbf{E}\times\mathbf{B}$ ion drifts operate in the opposite sense to transport plasma from the bottomside ionosphere to the topside ionosphere. This difference between the topside and bottomside ionosphere in response to upward ion drifts is due to the vertical advection term $v\frac{\partial N_e}{\partial h}$ operating oppositely in the two cases. For an upward velocity V the advective term will tend to have opposite effects on electron density changes in the bottom and topside ionosphere because of different signs of $\frac{\partial N_e}{\partial h}$. Generally, an upward plasma velocity increases electron density in the upper ionosphere and decreases electron density in the bottom ionosphere. Neutral winds also operate in a similar way to change electron densities at different altitudes; that is, poleward (equatorward) winds push ionosphere downward (upward) and increase electron density in the bottomside (topside) ionosphere but decrease (increase) electron density in the topside (bottomside) ionosphere.

In the topside ionosphere, $\mathbf{E}\times\mathbf{B}$ ion drifts become the dominant term responsible for SED; this term is partially offset by neutral winds and ambipolar diffusion. The main part of TEC is from the topside ionosphere and particularly the region from the F_2 peak to one scale height above the F_2 peak. It should be emphasized here that $\mathbf{E}\times\mathbf{B}$ upward ion drifts alone cannot increase TEC dramatically, since they can only change the altitude distribution of electron density by transporting plasmas from the bottom to topside ionosphere. They ultimately increase ion densities because the ions are moved up to an altitude in which recombination is much reduced. In summary, the SED in TEC is mainly generated by local upward $\mathbf{E}\times\mathbf{B}$ in the presence of reduced chemical recombination. *Wang et al.* [2012] compared the results from the stand-alone TIEGCM with

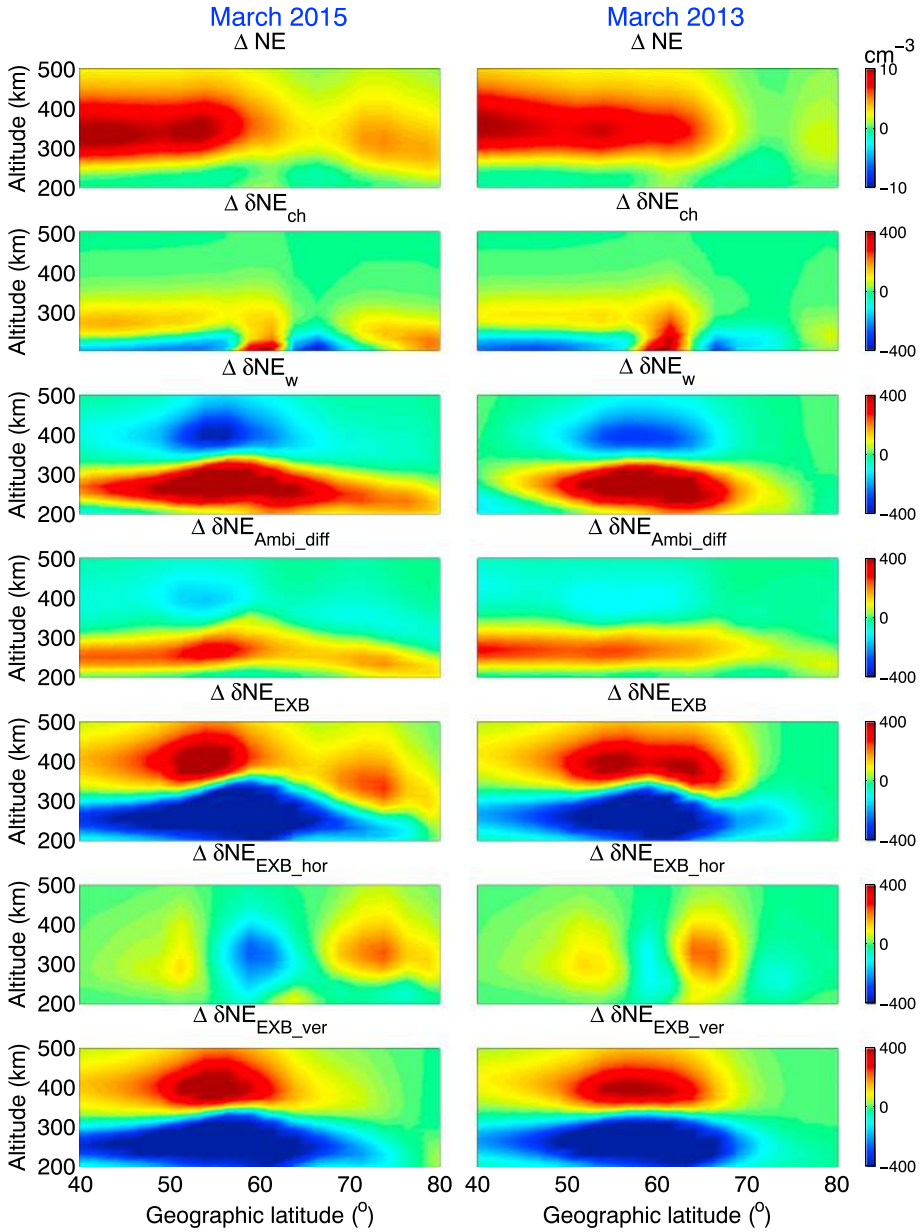

Figure 9. Modeled altitude versus geographic latitude plots of the absolute difference in electron density between storm time (17 March) and quiet time (16 March) (ΔNE, first row, in units of 10^5 cm^{-3}) and electron density change rate caused by these terms: production and loss rates ($\Delta\delta NE_{ch}$, in units of cm^{-3} s^{-1}), neutral wind transport ($\Delta\delta NE_{w}$, in units of 10^5 cm^{-3} s^{-1}), ambipolar diffusion ($\Delta\delta NE_{Ambi_diff}$, in units of cm^{-3} s^{-1}), electric fields transport ($\Delta\delta NE_{E\times B}$, in units of cm^{-3} s^{-1}), electric field horizontal transport ($\Delta\delta NE_{E\times B_hor}$, in units of cm^{-3} s^{-1}), and electric field vertical transport ($\Delta\delta NE_{E\times B_ver}$, in units of cm^{-3} s^{-1}) at 2000 UT for (left column) March 2015 and (right column) March 2013.

and without SAPS. They showed that SAPS caused negligible changes in ion density in the dayside convection throat region and reduce electron content in the later afternoon sector along the flow channel.

In current analysis, we mainly focused on polar ionosphere variability during the interval between 1700 and 2300 UT on 17 March. The storm commenced at around 0600 UT. There is about a half day of ionospheric preconditioning, which could lead to the different response of the ionosphere to these two storms that is shown in Figure 3. Figure 2 shows that the solar wind driving conditions are different for these two storms, with stronger geomagnetic forcing during the 2015 event. It is expected that stronger Joule heating occurred during the 2015 storm. This stronger Joule heating in the 2015 event perturbed the neutral atmosphere to

a greater extent, resulting in a larger depletion in electron density at high latitudes. That is why the SED/TOI is weaker for the 2015 event than that in the 2013 event.

In addition, ionosphere conductance was changed as a result of electron density changes, so magnetosphere energy input into the ionosphere was modified accordingly. Electron density changes can also feed back into the neutral winds through ion-neutral collisions and thus influence the location of the neutral composition perturbations. These prior ionosphere and thermosphere state changes certainly impact the current ionosphere state. However, it is difficult to assess the extent to which the current ionosphere is affected by preconditioning, due to the complex nonlinear magnetosphere-ionosphere-thermosphere interactions in this coupled system.

5. Concluding Remarks

Both the GPS TEC observations and TIEGCM simulations were used in this work to investigate the polar ionosphere response to two geomagnetic storms that occurred on 17 March 2013 and 2015. These two storms almost commenced at the same UT but have different intensities. The main findings are as follows:

1. These two March storms share similarities in that negative ionosphere storm effects dominated the high latitude ionosphere and the middle- and low-latitude ionospheric TEC were enhanced late in the storm main phase. The ionospheric response exhibited hemispheric asymmetry with a more pronounced negative storm effect in the Northern Hemisphere.
2. Upward $\mathbf{E} \times \mathbf{B}$ ion drifts are most important in generating the SED in the topside ionosphere and are offset by antisunward neutral winds and ambipolar diffusion effects. In the bottomside ionosphere, neutral winds play a major role in producing SED. Horizontal $\mathbf{E} \times \mathbf{B}$ ion drifts play an essential role in transporting plasma from the throat region into the polar cap to form TOIs.
3. Disagreements exist between model results and GPS TEC observations. An electron density "hole" in the throat region occurred in GPS TEC observations for both storm events, which was not captured by the TIEGCM.

Acknowledgments
This work is supported by NASA LWS grants NNX14AE06G and NNX15AB83G and NASA HGI grant NNX12AJ54G. The National Center for Atmospheric Research is sponsored by the National Science Foundation. The TIEGCM output data used in this paper are accessible upon request (jingliu@ucar.edu). Observations and analysis at MIT Haystack Observatory are supported by cooperative agreement AGS-1242204 between the National Science Foundation and the Massachusetts Institute of Technology. GPS TEC data products and access through the Madrigal distributed data system (http://madrigal.haystack.mit.edu/madrigal/) are provided to the community by the Massachusetts Institute of Technology under support from U.S. National Science Foundation grant AGS-1242204. The solar wind parameters are obtained from the OMNI 2 database (ftp://spdf.gsfc.nasa.gov/pub/data/omni/high_res_omni/).

References

Anderson, D. N. (1976), Modeling the midlatitude *F*-region ionospheric storm using east-west drift and a meridional wind, *Planet. Space Sci.*, *24*, 69–77, doi:10.1016/0032-0633(76)90063-5.

Belehaki, A., and I. Tsagouri (2002), On the occurrence of storm-induced nighttime ionization enhancements at ionospheric middle latitudes, *J. Geophys. Res.*, *107*(A8), 1209, doi:10.1029/2001JA005029.

Buonsanto, M. J. (1995a), Millstone Hill incoherent scatter *F* region observations during the disturbances of June 1991, *J. Geophys. Res.*, *100*, 5743–5755, doi:10.1029/94JA03316.

Buonsanto, M. J. (1995b), A case study of the ionospheric storm dusk effect, *J. Geophys. Res.*, *100*, 23,857–23,869, doi:10.1029/95JA02697.

Buonsanto, M. J. (1999), Ionospheric storms: A review, *Space Sci. Rev.*, *88*, 563–601, doi:10.1023/A:1005107532631.

Burns, A. G., W. Wang, T. L. Killeen, and S. C. Solomon (2004), A "tongue" of neutral composition, *J. Atmos. Sol. Terr. Phys.*, *66*, 1457–1468, doi:10.1016/j.jastp.2004.04.009.

Cherniak, L., and I. Zakharenkova (2015), Dependence of the high-latitude plasma irregularities on the auroral activity indices: A case study of the 17 March 2015 geomagnetic storm, *Earth Planets Space*, *67*, 151, doi:10.1186/s40623-015-0316x.

David, M., J. J. Sojka, R. W. Schunk, M. W. Liemohn, and A. J. Coster (2011), Dayside midlatitude ionospheric response to storm time electric fields: A case study for 7 September 2002, *J. Geophys. Res.*, *116*, A12302, doi:10.1029/2011JA016988.

Deng, Y., and A. J. Ridley (2006), Role of vertical ion convection in the high-latitude ionospheric plasma distribution, *J. Geophys. Res.*, *111*, A09314, doi:10.1029/2006JA011637.

Evans, J. V. (1973), The causes of storm-time increases of the *F*-layer at midlatitudes, *J. Atmos. Terr. Phys.*, *35*, 593–616, doi:10.1016/0021-9169(73)90191-8.

Foster, J., W. Rideout, B. Sandel, W. Forrester, and F. Rich (2007), On the relationship of SAPS to storm-enhanced density, *J. Atmos. Sol. Terr. Phys.*, *69*, 303–313, doi:10.1016/j.jastp.2006.07.021.

Foster, J. C. (1993), Storm-time plasma transport at middle and high latitudes, *J. Geophys. Res.*, *98*, 1675–1689, doi:10.1029/92JA02032.

Fuller-Rowell, T. (2011), Storm-time response of the thermosphere–ionosphere system, in *Aeronomy of the Earth's Atmosphere and Ionosphere*, *IAGA Spec. Sopron Book Ser.*, vol. 2, edited by M. A. Abdu and D. Pancheva, pp. 419–434, Springer, Dordrecht, Netherlands, doi:10.1007/978-94-007-0326-1_32.

Hagan, M. E., and J. M. Forbes (2002), Migrating and nonmigrating diurnal tides in the middle and upper atmosphere excited by tropospheric latent heat release, *J. Geophys. Res.*, *107*(D24), 4754, doi:10.1029/2001JD001236.

Hagan, M. E., and J. M. Forbes (2003), Migrating and nonmigrating semidiurnal tides in the upper atmosphere excited by tropospheric latent heat release, *J. Geophys. Res.*, *108*(A2), 1062, doi:10.1029/2002JA009466.

Heelis, R. A., J. J. Sojka, M. David, and R. W. Schunk (2009), Storm time density enhancements in the middle-latitude dayside ionosphere, *J. Geophys. Res.*, *114*, A03315, doi:10.1029/2008JA013690.

Huang, C.-S., J. C. Foster, L. P. Goncharenko, P. J. Erickson, W. Rideout, and A. J. Coster (2005), A strong positive phase of ionospheric storms observed by the Millstone Hill incoherent scatter radar and global GPS network, *J. Geophys. Res.*, *110*, A06303, doi:10.1029/2004JA010865.

Kelley, M. C., M. N. Vlasov, J. C. Foster, and A. J. Coster (2004), A quantitative explanation for the phenomenon known as storm-enhanced density, *Geophys. Res. Lett.*, *31*, L19809, doi:10.1029/2004GL020875.

King, J. H., and N. E. Papitashvili (2005), Solar wind spatial scales in and comparisons of hourly Wind and ACE plasma and magnetic field data, *J. Geophys. Res.*, *110*, A02104, doi:10.1029/2004JA010649.

Lei, J., W. Wang, A. G. Burns, S. C. Solomon, A. D. Richmond, M. Wiltberger, L. P. Goncharenko, A. Coster, and B. W. Reinisch (2008), Observations and simulations of the ionospheric and thermospheric response to the December 2006 geomagnetic storm: Initial phase, *J. Geophys. Res.*, *113*, A01314, doi:10.1029/2007JA012807.

Liu, J., T. Nakamura, L. Liu, W. Wang, N. Balan, T. Nishiyama, M. R. Hairston, and E. G. Thomas (2015), Formation of polar ionospheric tongue of ionization during minor geomagnetic disturbed conditions, *J. Geophys. Res. Space Physics*, *120*, 6860–6873, doi:10.1002/2015JA021393.

Liu, J., W. Wang, A. Burns, X. Yue, S. Zhang, Y. Zhang, and C. Huang (2016), Profiles of ionospheric storm-enhanced density during the 17 March 2015 great storm, *J. Geophys. Res. Space Physics*, *121*, 727–744, doi:10.1002/2015JA021832.

Lockwood, M., and H. C. Carlson (1992), Production of polar cap electron density patches by transient magnetopause reconnection, *Geophys. Res. Lett.*, *19*, 1731–1734, doi:10.1029/92GL01993.

Mendillo, M., M. D. Papagiannis, and J. A. Klobuchar (1972), Average behavior of the midlatitude *F*-region parameters N_T, N_{max} and τ during geomagnetic storms, *J. Geophys. Res.*, *77*, 4891–4895, doi:10.1029/JA077i025p04891.

Moen, J., X. C. Qiu, H. C. Carlson, R. Fujii, and I. W. McCrea (2008), On the diurnal variability in F_2-region plasma density above the EISCAT Svalbard radar, *Ann. Geophys.*, *26*, 2427–2433, doi:10.5194/angeo-26-2427-2008.

Papagiannis, M. D., M. Mendillo, and J. A. Klobuchar (1971), Simultaneous storm-time increases of the ionospheric total electron content and the geomagnetic field in the dusk sector, *Planet. Space Sci.*, *19*, 503–511, doi:10.1016/0032-0633(71)90166-8.

Qian, L., A. G. Burns, B. A. Emery, B. Foster, G. Lu, A. Maute, A. D. Richmond, R. G. Roble, S. C. Solomon, and W. Wang (2014), The NCAR TIE-GCM, in *Modeling the Ionosphere–Thermosphere System*, edited by J. Huba, R. Schunk and G. Khazanov, pp. 73–83, John Wiley, Chichester, U. K., doi:10.1002/9781118704417.ch7.

Richmond, A. D., E. C. Ridley, and R. G. Roble (1992), A thermosphere/ionosphere general circulation model with coupled electrodynamics, *Geophys. Res. Lett.*, *19*, 601–604, doi:10.1029/92GL00401.

Rideout, W., and A. Coster (2006), Automated GPS processing for global total electron content data, *GPS Solut.*, *10*, 219–228, doi:10.1007/s10291-006-0029-5.

Rishbeth, H., R. A. Heelis, J. J. Makela, and S. Basu (2010), Storming the Bastille: The effect of electric fields on the ionospheric *F*-layer, *Ann. Geophys.*, *28*, 977–981, doi:10.5194/angeo-28-977-2010.

Roble, R. G., and E. C. Ridley (1987), An auroral model for the NCAR thermospheric general circulation model (TGCM), *Ann. Geophys.*, *87*, 369–382.

Roble, R. G., E. C. Ridley, A. D. Richmond, and R. E. Dickinson (1988), A coupled thermosphere/ionosphere general circulation model, *Geophys. Res. Lett.*, *15*, 1325–1328, doi:10.1029/GL015i012p01325.

Rodger, A. S., M. Pinnock, J. R. Dudeney, K. B. Baker, and R. A. Greenwald (1994), A new mechanism for polar patch formation, *J. Geophys. Res.*, *99*, 6425–6436, doi:10.1029/93JA01501.

Sato, T. (1959), Morphology of ionospheric F_2 disturbances in the polar regions: A linkage between polar patches and plasmaspheric drainage plumes, *Rep. Ionos. Res. Space Res. Jpn.*, *131*, 91.

Tsurutani, B., et al. (2004), Global dayside ionospheric uplift and enhancement associated with interplanetary electric fields, *J. Geophys. Res.*, *109*, A08302, doi:10.1029/2003JA010342.

Wang, W., E. R. Talaat, A. G. Burns, B. Emery, S. Hsieh, J. Lei, and J. Xu (2012), Thermosphere and ionosphere response to subauroral polarization streams (SAPS): Model simulations, *J. Geophys. Res.*, *117*, A07301, doi:10.1029/2012JA017656.

Weimer, D. R. (2005), Improved ionospheric electrodynamic models and application to calculating Joule heating rates, *J. Geophys. Res.*, *110*, A05306, doi:10.1029/2004JA010884.

Zhang, Q. H., et al. (2011), On the importance of interplanetary magnetic field $|B_y|$ on polar cap patch formation, *J. Geophys. Res.*, *116*, A05308, doi:10.1029/2010JA016287.

Zhang, Q. H., B.-C. Zhang, J. Moen, M. Lockwood, I. W. McCrea, H.-G. Yang, H.-Q. Hu, R.-Y. Liu, S.-R. Zhang, and M. Lester (2013a), Polar cap patch segmentation of the tongue of ionization in the morning convection cell, *Geophys. Res. Lett.*, *40*, 2918–2922, doi:10.1002/grl.50616.

Zhang, Q. H., et al. (2013b), Direct observations of the evolution of polar cap ionization patches, *Science*, *339*, 1597–1600, doi:10.1126/science.1231487.

Zhang, Q. H., M. Lockwood, J. C. Foster, S.-R. Zhang, B.-C. Zhang, I. W. McCrea, J. Moen, M. Lester, and J. M. Ruohoniemi (2015), Direct observations of the full Dungey convection cycle in the polar ionosphere for southward interplanetary magnetic field conditions, *J. Geophys. Res. Space Physics*, *120*, 4519–4530, doi:10.1002/2015JA021172.

Zou, S., M. B. Moldwin, A. J. Ridley, M. J. Nicolls, A. J. Coster, E. G. Thomas, and J. M. Ruohoniemi (2014), On the generation/decay of the storm-enhanced density plumes: Role of the convection flow and field-aligned ion flow, *J. Geophys. Res. Space Physics*, *119*, 8543–8559, doi:10.1002/2014JA020408.